Composites Part B 218 (2021) 108931

Contents lists available at ScienceDirect

Composites Part B

journal homepage: www.elsevier.com/locate/composites

Damage propagation in short fiber thermoplastic composites analyzed through coupled 3D experiments and simulations

Imad Hanhan, Michael D. Sangid *

School of Aeronautics and Astronautics, Purdue University, West Lafayette, IN, 47907, USA

ARTICLE INFO

Keywords:
Polymer–matrix composites (PMCs)
Microstructures
Finite element analysis (FEA)
Radiography
Injection molding

ABSTRACT

Due to the complex nature of the heterogeneous microstructures of short fiber composites, computationally predicting their mechanical behavior, especially past the elastic regime and into the damage initiation and progression regimes, is very challenging. Matrix cracking has notably been difficult to predict because it can propagate in different manners, such as fiber mediated interfacial cracking and conoidal cracking, which have not been well understood. Therefore, this work couples *in-situ* X-ray micro tomography experiments with a finite element simulation of the exact microstructure to enable a sub-fiber 3D microstructural study by tracking damage propagation and computing the local stresses and strains in the microstructure. Here we show the role of shear stress in interfacial cracking (and how it differs from debonding), the role of hydrostatic stress in conoidal cracking, and the role of environmental damage in longitudinal fiber breakage. In doing so, this work gives insight into the stress states resulting in non-linear damage propagation in thermoplastic fiber composites.

1. Introduction

Short fiber composites have become popular in many engineering applications due to their relatively low cost of manufacturing, especially for complicated 3D geometries. The microstructure of these composites, which is typically characterized by parameters like the fiber volume fraction, fiber orientation distribution, fiber length distribution, and porosity volume fraction, is dependent on the manufacturing parameters [1–3] and strongly influences the mechanical performance [4–8]. Therefore, researchers have developed techniques and tools to not only predict the microstructure of these composites based on their manufacturing parameters [9–11], but to also try and predict the mechanical response using these microstructural parameters [12–14].

However, predicting the complete mechanical behavior of these short fiber composites is challenging due to the heterogeneity of the microstructure and its behavior past the elastic regime. Therefore, most predictive capabilities have been focused on the elastic loading regime [12,15], before damage initiation or progression has occurred. These anisotropic elastic properties can be predicted using fiber volume fraction, orientation, and length distributions. Some recent work has been done in predicting the bulk mechanical response past the elastic regime, towards the strength predictions of short fiber composites, using phenomenological damage parameters and/or homogenization [16–18].

Within the microstructure of thermoplastic composites when loaded past the elastic regime, damage initiation is usually observed in the form of microvoid nucleation in the thermoplastic matrix, specifically at fiber tips, which early works have shown through *in-situ* scanning electron microscopy [19,20]. In understanding and predicting this behavior, the two main challenges for these composites are the highly non-linear response of the thermoplastic matrix (which experiences significant plasticity) and its interaction with fibers of varying lengths and orientations [21]. For damage initiation, a previous work analyzed a 3D experiment (between 0% and 50% of failure) along with a coupled simulation matching those experimental conditions to show that microvoid nucleation during damage initiation is related to localized high hydrostatic stress in the matrix at fiber tips [22]. However, it is unclear how microvoids evolve during damage progression (after 50% of failure), especially in 3D.

One historically observed behavior during both damage initiation and propagation is debonding of the fiber and the matrix [23]. This mechanism, sometimes called interfacial debonding or mode β [24], is akin to adhesive bond failure. In an effort to retain the integrity of a fiber's load bearing ability, researchers have worked to develop a number of different techniques to improve the adhesion of the fiber and the matrix through fiber surface pre-treatments [25]. These fiber pre-treatments create a chemical reaction at the surface of the fiber

* Corresponding author.
E-mail address: msangid@purdue.edu (M.D. Sangid).

https://doi.org/10.1016/j.compositesb.2021.108931
Received 13 May 2020; Received in revised form 8 April 2021; Accepted 18 April 2021
Available online 21 April 2021

with a thickness that varies depending on the material system; for E-glass fibers and a polypropylene matrix, it is expected to be on the order of 100 nm [26]. The development of such fiber treatments has proven to be very successful, making debonding extremely unlikely (occurring mainly in the early loading sequence for a small fraction of fibers which may have had unfavorable bonding conditions) as has been shown through fractography [19,27]. With well bonded fibers, debonding is not dominant during damage progression. Instead, due to strong adhesion to the fiber, interfacial microcracking of the matrix along fiber sides (akin to cohesive bond failure) is one of the main observed behaviors during damage propagation, and it occurs late in the monotonic loading sequence (at about 75% of the failure load) [19]. This is hypothesized to be a result of a shear stress concentration along the fiber side [19]. However, while debonding may not be widespread, it is unclear if localized debonding could still be responsible for some portion of damage propagation, as well as how the driving forces differ between debonding and interfacial matrix cracking.

Another observed behavior active during damage progression is cracking through the matrix in a manner that is not along a fiber edge, first referred to as 'zigzag' matrix microcracking, which activates to connect and coalesce microvoids and interfacial matrix cracks [19]. To try to understand this mechanism of matrix cracking, researchers isolated a single fiber in a matrix and analyzed the behavior of matrix cracking through surface measurements. It was found that even with a single fiber in a matrix, there exists a mechanism of matrix cracking which is not necessarily fiber interface mediated. This observed mechanism has been described more broadly as mode γ cracking [24] and fiber avoidance cracking [28,29], or more specifically by its shape, such as penny [30], conical [31,32], conoidal (a mix of conical and flat) [33], and helicoidal [33]. In this work, this form of matrix cracking, that is not fiber interface mediated, will be simply referred to as conoidal matrix cracking.

Lastly, fiber breakage is sometimes observed during damage progression. In general, fiber breakage is not a common occurrence in short fiber reinforced thermoplastic composites and is either not observed [19] or considered to be rare [34]. While uncommon, some fiber breakage events have been documented for these material systems, and are generally characterized as either (1) transverse breaks of fibers that are well aligned with the loading direction (which are well understood), or (2) longitudinal breaks of fibers that are misaligned with the loading direction, which are less common and not well understood [35].

From a prediction standpoint, interfacial matrix cracking along a fiber (and how it differs from debonding), conoidal cracking through the matrix, and longitudinal fiber breakage have been challenging to predict due to a lack of understanding of the physical phenomena that govern their behavior. Specifically, conoidal matrix cracking has proven to be challenging for researchers to predict because of its apparent stochastic nature. In an attempt to predict this conoidal matrix cracking behavior, researchers studied a single isolated perfectly aligned fiber in an epoxy matrix in 2D, and through a modified Rice and Tracey model were able to successfully predict the angle between a conoidal matrix crack and the fiber (within 2°) [32]. However, there has not been a clear and comprehensive explanation of the interaction of interfacial cracks and conoidal cracks, especially in 3D for a thermoplastic matrix, other than they might be accelerated by shear stress [28,36]. Understanding the physical phenomenon that drives conoidal matrix cracking and interfacial matrix cracking along a fiber, especially if it results in major damage coalescence, as well as exposing possible causes for longitudinal fiber breakage of misaligned fibers, would allow for more accurate predictions of the complete mechanical behavior of short fiber reinforced thermoplastics.

Therefore, this work coupled an *in-situ* X-ray micro-computed tomography (μ-CT) experiment (shown in Fig. 1) analyzed at 50%, 75%, and 85% of failure, with a 3D finite element method (FEM) simulation of the exact microstructure matching those experimental conditions, including all fibers, all manufacturing induced pores, and non-linear behavior in the thermoplastic matrix, in order to characterize the behavior of microstructural damage propagation and compare it to the computed stresses in the quasi-static simulation. Specifically, locations of damage initiation within the ductile fracture zone were tracked as the material was loaded, and processed through robust image processing and segmentation procedures to extract each individual fiber and pore [22]. The experimental 3D behavior of matrix cracking was analyzed for regions of cracking along fiber edges (which could be interfacial matrix cracking or debonding), as well as conoidal matrix cracking. The finite element simulation, which contained over 7 million elements, computed the full stress field at a static snapshot directly after 50% of failure, and allowed for a direct comparison to the experimentally observed damage progression within the microstructure.

This paper will first describe the material, followed by the experimental procedure and its corresponding tomography post-processing. The methods of the FEM simulation will then be described, followed by the results and discussions of four damage mechanisms active during damage propagation (interfacial matrix cracking, debonding, conoidal matrix cracking, and fiber breakage). Experimentally, these mechanisms were analyzed between $0.5\varepsilon_f$ (50% of the macroscopic strain to failure) and $0.85\varepsilon_f$ (85% of the macroscopic strain to failure), and a region of damage coalescence which eventually led to major ductile failure in the ductile fracture zone was determined. While previous work by the authors investigated damage initiation in short fiber thermoplastic composites [22], the present work will be solely focused on damage propagation (crack growth) in the same material.

Through the coupled experiment and simulation analysis, this work provides insight into the physical stress states that govern cracking along a fiber edge and conoidal matrix cracking. Instead of applying a specific failure criteria, such as Von Mises for the matrix, each component of simulated stress (including hydrostatic and maximum principal) was analyzed to provide insight to the underlying physics guiding crack growth in varying mechanisms. Specifically, this paper will present two locations of cracking along a fiber edge, where one was determined to be interfacial matrix cracking, while the other was determined to be debonding. Next, two locations of conoidal matrix cracking will be shown. Lastly, fiber breakage was analyzed and categorized as either transverse breakage of a well aligned fiber, or longitudinal breakage of a misaligned fiber. Only one fiber was found to break in a longitudinal fashion, and is also explored in this paper. Overall, the results of this work provide a comprehensive understanding of the physics governing the coalescence of damage initiation sites within the complex and heterogeneous microstructure of short fiber reinforced thermoplastics, increasing the understanding of the micromechanical response past damage initiation and propelling engineers towards strength and failure predictions of these short fiber composites.

2. Materials and methods

2.1. Composite material

The material used in this work was a polypropylene matrix reinforced with 30% by weight E-glass fibers which are approximately 10 μm in diameter. The glass fibers were pre-treated with a tailored silane solution to promote adhesion between the fibers and the polymer. The composite material was injection molded into a cylindrical rod with a diameter of 1.27 cm and a length of 45.72 cm, where the injection molding flow direction was in the length direction of the rod (Z). From the injection molded rod, a smaller dog-bone shaped specimen was machined from the center with a grip diameter of approximately 6.3 mm, a gauge section diameter of 2.5 mm, and a gauge section length of 5 mm, where the loading direction was in the Z direction.

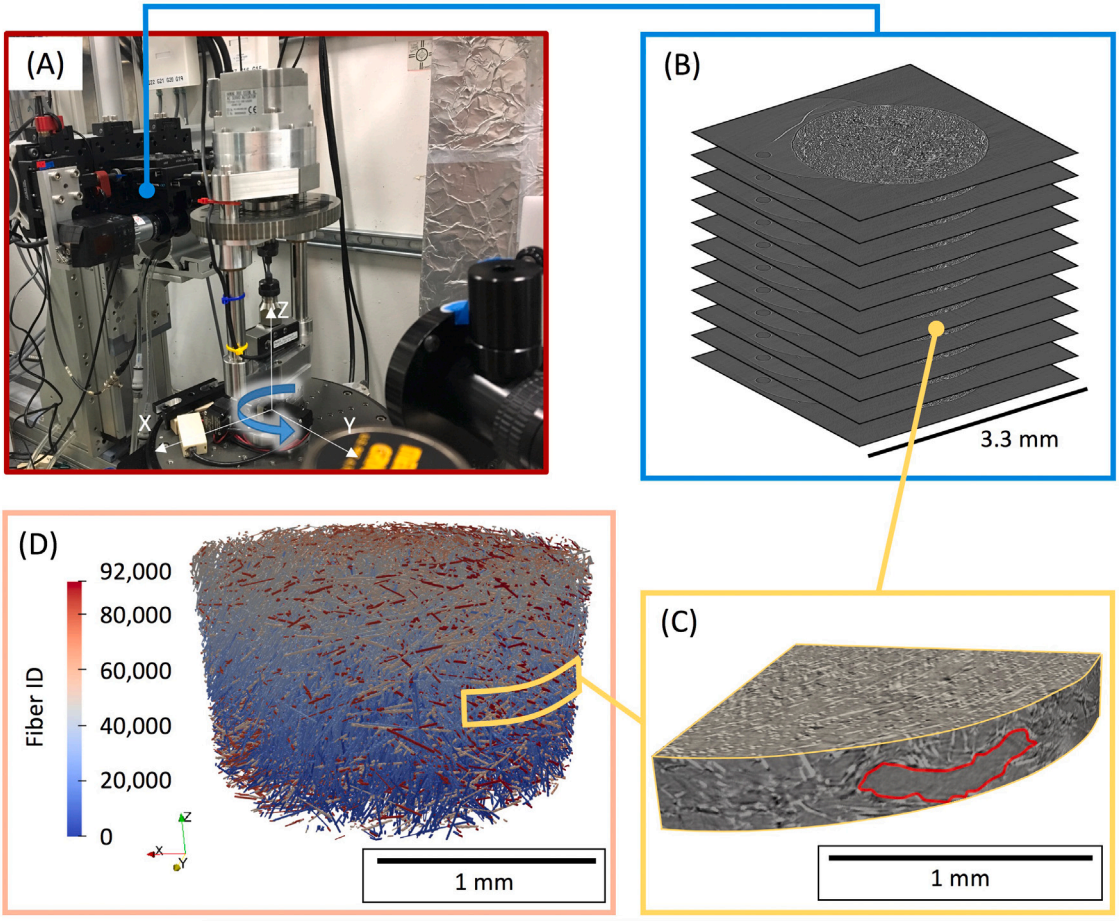

Fig. 1. An overview of the *in-situ* study where (A) shows the *in-situ* loading set-up with the miniature load frame, (B) shows a sample of the reconstructed tomography images, (C) shows the ductile fracture zone just before fracture, and (D) shows a sample of the fibers detected in the microstructure (cropped away from the edges by 340 μm radially). (For interpretation of the references to color in this figure legend, the reader is referred to the web version of this article.)

2.2. Experimental details

An *in-situ* tomography study was conducted at the Advanced Photon Source at Argonne National Laboratory using the assembly shown in Fig. 1A. Each X-ray projection, which was acquired with an X-ray energy of 25 keV, was collected on an area detector placed 75 mm downstream from the specimen with an exposure time of 100 ms collected every 0.12°. The assembly, which included the specimen placed within a custom miniature load frame, was rotated at 0.5°/s through a 180° range. The use of synchrotron X-rays allowed for a μ-CT scan of a volume with dimensions 3.33 by 3.33 by 1.61 mm to be acquired with a pixel size of 1.3 μm in about 6 min. The 1500 X-ray projections acquired during each tomography scan were reconstructed using TomoPy, which is a python-based framework developed by scientists at Argonne National Laboratory [37]. This work used the default Gridrec algorithm, which is a direct Fourier-based method [38]. In implementing TomoPy in this work, it was necessary to first determine the appropriate reconstruction center of the tomography images, which is done through a trial-and-error approach through built in TomoPy functions that can be found in the TomoPy documentation. Lastly, it is possible to exclude certain projections when reconstructing using TomoPy; in this work, it was necessary to exclude projections that were obstructed by the load frame columns. Due to TomoPy's ability to handle missing projections, this does not reduce the quality of the reconstructions [39]. Once fully reconstructed, the acquired tomography scan results in 2D images which stack to form a 3D image, as shown in Fig. 1B.

Using the custom miniature load frame, the specimen was loaded in tension by incrementally displacing the cross-head 0.01 mm at a quasi-static cross-head displacement rate of approximately 0.2 mm/min, holding the cross-head displacement, and acquiring an *in-situ* tomography scan. Once the scan was completed, the cross-head was displaced 0.01 mm again and held for the next scan. The 3D time-lapse tomography data allowed for the observation of damage (Fig. 1C) and the extraction of microstructural features, including each fiber (Fig. 1D). The exterior of the specimen was painted with a black and white speckle pattern and monitored using an optical camera at each increment in order to allow for the computation of macroscopic strain through digital image correlation which was conducted using VIC-2D. In VIC-2D, the graphical user interface allows for a straightforward selection of the portion within the image that is analyzed for relative motion and the corresponding computed strain. A total of 58 scans were acquired between the unloaded state and final fracture, which occurred at 5.77% macroscopic strain.

2.3. Experimental post-processing

The tomography images acquired at $0.99\varepsilon_f$ (99% of the macroscopic strain to failure) were inspected using ImageJ, and the ductile fracture zone (the region of ductile fracture which transitions to brittle fracture just before final failure [19]) was determined [22]. Using six face 2D cross-correlation in Matlab (with function normxcorr2), the ductile fracture zone was traced from $0.99\varepsilon_f$ back to the microstructure at $0.85\varepsilon_f$, $0.75\varepsilon_f$, $0.5\varepsilon_f$, $0.3\varepsilon_f$, and 0 load.

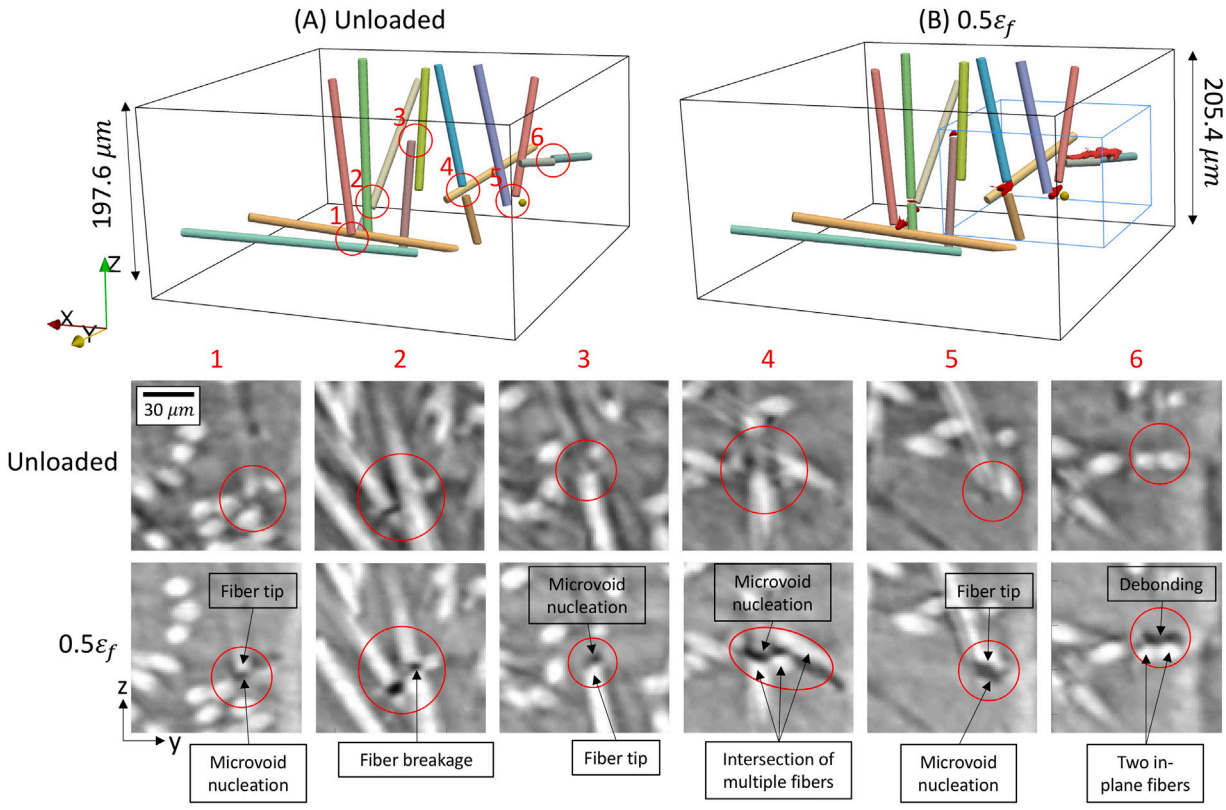

Fig. 2. An overview of the damage initiation events labeled 1 through 6 that occurred within the ductile fracture zone visualized at (A) the unloaded state, and at (B) $0.5\varepsilon_f$, with a blue box indicating the region of interest for the damage propagation analysis, and with corresponding tomography images at each of the 6 locations, where sites labeled 1–5 were microvoid nucleation, and site 6 was early debonding.

The 3D tomography images at each load step were adjusted first using median scaling [40], followed by three general procedures: fiber detection, porosity detection, and free surface detection. Fiber detection was conducted using a combined 2D/3D iterative approach developed by Agyei and Sangid [41]. The algorithm iteratively enhances and segments each 2D image in the stack of reconstructed μ-CT images. The cross-section of each fiber on each slice is fitted using an elliptical fit, and this ellipse data is stacked and undergoes a number of 3D segmentation steps [41]. The segmentation of the fibers was inspected and corrections to the automated segmentation were conducted using ModLayer [42]. In ModLayer, consecutive 2D slices of the 3D tomography image can be viewed on the left side of the graphical user interface, with the multi-class fiber segmentation on the right. ModLayer was then used to scroll, zoom, and pan through the linked images to evaluate and fix any inaccuracies within the multi-class fiber segmentation [42].

Fibers in the experimental analysis, which played a role by interacting with damage events within the ductile fracture zone, were rendered in ParaView using a cylindrical fit of the detected fibers to aid in visual interpretation. These can be seen in Fig. 2A and B at the unloaded state and at $0.5\varepsilon_f$, respectively. An in-depth 3D reconstruction of the surface of certain fibers of interest was conducted by first segmenting pixels in the region of the fiber with normalized intensity greater than 0.65 followed by inspection and segmentation correction using ModLayer [42]. The manufacturing induced porosity in the unloaded state, as well as microvoids that nucleated after loading, were detected using Weka machine learning segmentation [43] and manually corrected using ModLayer [42]. Weka segmentation is part of the Fiji image processing package [44], and allows the user to point and click within the graphical user interface in order to train the Weka segmentation module for portions of the image that are voids. Additionally, there is support for 3D images, which are accomplished by repeating the same point and click training on consecutive 2D slices. The Weka segmentation module can be evaluated by running the detection, applying an overlay of the segmentation result, and visually observing imperfections in the detection, which can be fixed through additional training. This procedure aided in the 3D interpretation of damage events as can be seen in Fig. 2B.

The specimen's free surface was determined through 2D image processing of each tomography slice using an in-house Matlab algorithm that utilized the intensity gradient at the free surface, and an initial estimate of the approximate center and radius of the cylindrical specimen [22]. This region was enhanced by mapping the intensity values from a range of 0 to 1 into a range of 0.4 to 0.9, converted to a binary image using a threshold of 0.655 of the median normalized intensity of the image (which accounts for X-ray energy fluctuations), dilated by a disk structural element with a radius of 4 pixels, and finally adjusted to fill any holes in the edge region [22].

Through analysis of the 3D tomography data from the unloaded state to $0.5\varepsilon_f$, six sites of damage initiation (crack initiation) were found and were tracked throughout loading. Of the six total sites of damage initiation, sites numbered 1–5 in Fig. 2 were associated with microvoid nucleation, and were discussed in the previous work up to $0.5\varepsilon_f$ [22]. Site 6 in Fig. 2 exhibited early debonding of two fibers with lengths of 42 μm and 56 μm, each forming an angle with the loading axes (Z) of 84.1° and 84.5°, respectively. A region of interest which contained damage initiation sites 4–6 (blue box in Fig. 2B) was chosen for the damage progression analysis in this work ($\varepsilon > 0.5\varepsilon_f$) because it was experimentally observed to (1) contain coalescence of all three damage initiation sites between $0.5\varepsilon_f$ and $0.85\varepsilon_f$, (2) led to the formation of the largest void at $0.85\varepsilon_f$ which also reached the free surface, and (3) eventually led to catastrophic failure (outlined in red in Fig. 1C just before fracture). This smaller region of interest within the ductile fracture zone is shown at the unloaded state, $0.5\varepsilon_f$, and $0.85\varepsilon_f$ (through 6 face 2D cross-correlation tracking) in Fig. 3A, B, and C, respectively.

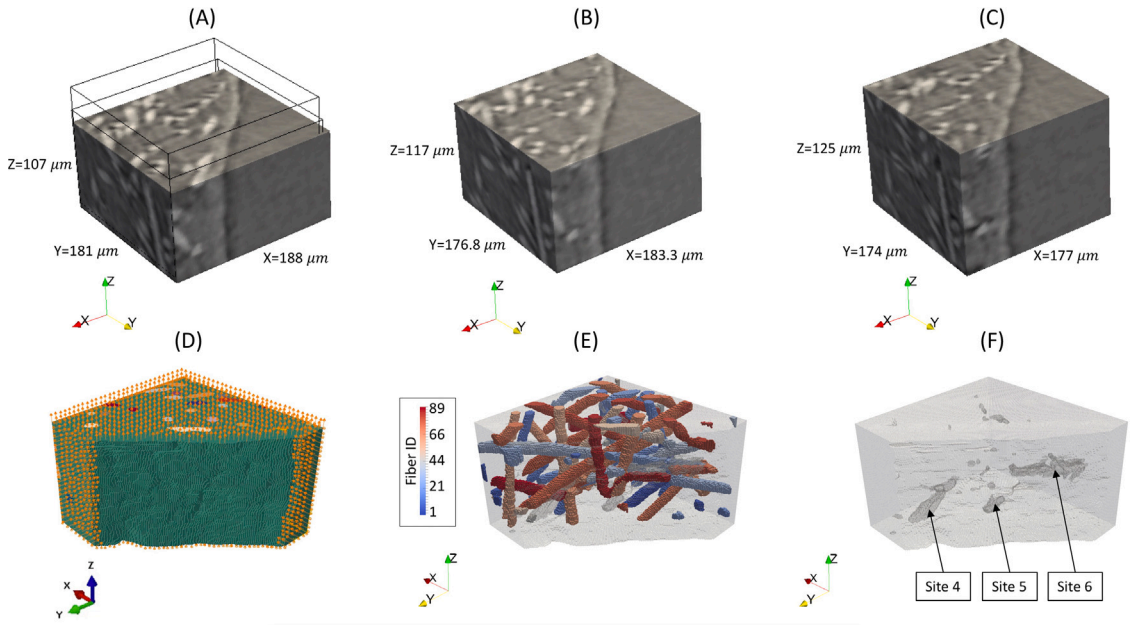

Fig. 3. An overview of the coupled experiment and simulation, where (A) is the region of interest for the damage propagation analysis at 0 load, (B) is the tracked region at $0.5\varepsilon_f$ that contained sites of damage initiation which grew significantly and coalesced in (C) at $0.85\varepsilon_f$. Simultaneously, (D) shows the simulation of the region of interest from $0.5\varepsilon_f$ to $0.85\varepsilon_f$, where the roller boundary conditions match the experimental results from (A) to (C). The detected fibers are shown in (E), and the voids present at $0.5\varepsilon_f$ can be seen in (F), where the three largest voids are the sites of damage initiation.

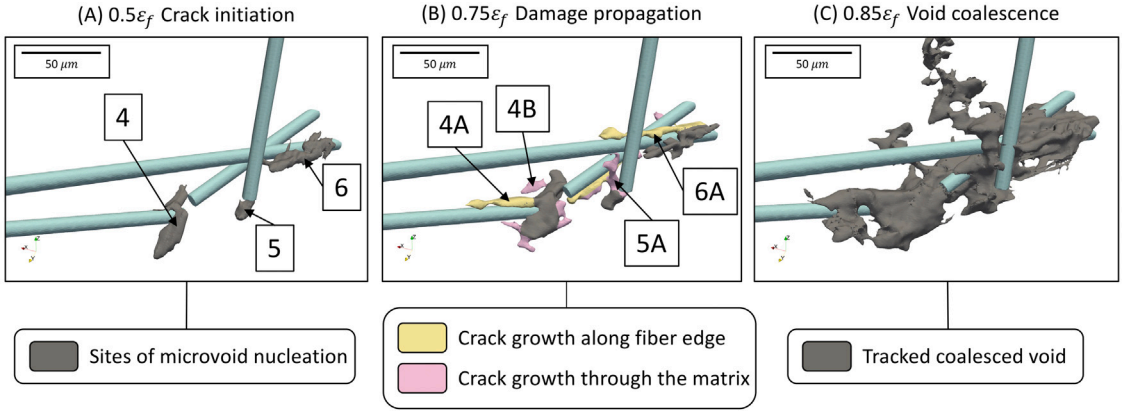

Fig. 4. The result of the experimental analysis of crack growth, where (A) shows crack initiation sites numbered 4, 5, and 6 at $0.5\varepsilon_f$, (B) shows crack growth sites 4A, 4B, 5A, and 6A at $0.75\varepsilon_f$ that are explored in this work, and (C) shows the large coalesced crack growth at $0.85\varepsilon_f$.

2.4. Simulation details

In the previous work, the microstructure at the unloaded state was simulated (before damage initiated or progressed) up to $0.5\varepsilon_f$ [22]. In this work, the experimental post-processing procedures were used to instantiate a 3D model of the exact microstructure at $0.5\varepsilon_f$ (after damage initiated but before it progressed and coalesced) in the region of interest, and simulated up to $0.85\varepsilon_f$. This includes the free surface shown in Fig. 3D, the fibers shown in Fig. 3E, as well as pores and nucleated microvoids shown in Fig. 3F, in order to create a simulation that can provide insight into the local stress states just after damage initiation.

Prior to meshing the microstructure, each voxel which corresponded to a void in the material was removed in ParaView using the threshold filter, and the remaining voxels were meshed using tetrahedral elements directly from the voxelated microstructure using the tetrahedralize filter which results in tetrahedral elements with ideal and uniform geometry [22]. This meshing procedure was conducted in ParaView, and resulted in perfect bonding between the fibers and the matrix, which can be assumed for fiber reinforced thermoplastics where the fibers have been pre-treated [19,22]. This ParaView mesh required post-processing in order to appropriately structure the node and element lists for compatibility with Abaqus, which in this work was done using an in-house Matlab algorithm. The meshed fiber elements were assigned linear elastic properties with an elastic modulus of 72.4 GPa and a Poisson's ratio of 0.2 [45,46]. The meshed matrix elements were simulated to include nonlinear plasticity through a multilinear isotropic hardening model based on experimental and simulation data in Ref. [47].

The experimental six face cross-correlation used to track the exact volume of tomography images between the unloaded state and $0.85\varepsilon_f$ was used to apply boundary conditions to the meshed microstructure at $0.5\varepsilon_f$. This corresponded to roller boundary conditions on the +X, −Y, and −Z surfaces, and roller boundary conditions with displacements of $X = 9.7$ μm on the −X surface (contraction in X), $Y = -5.2$ μm on the +Y surface (contraction in Y), and $Z = 20$ μm on the +Z surface (expansion in Z). These boundary conditions, which are visualized in Fig. 3D, effectively reproduce the same tension in the Z and Poisson's

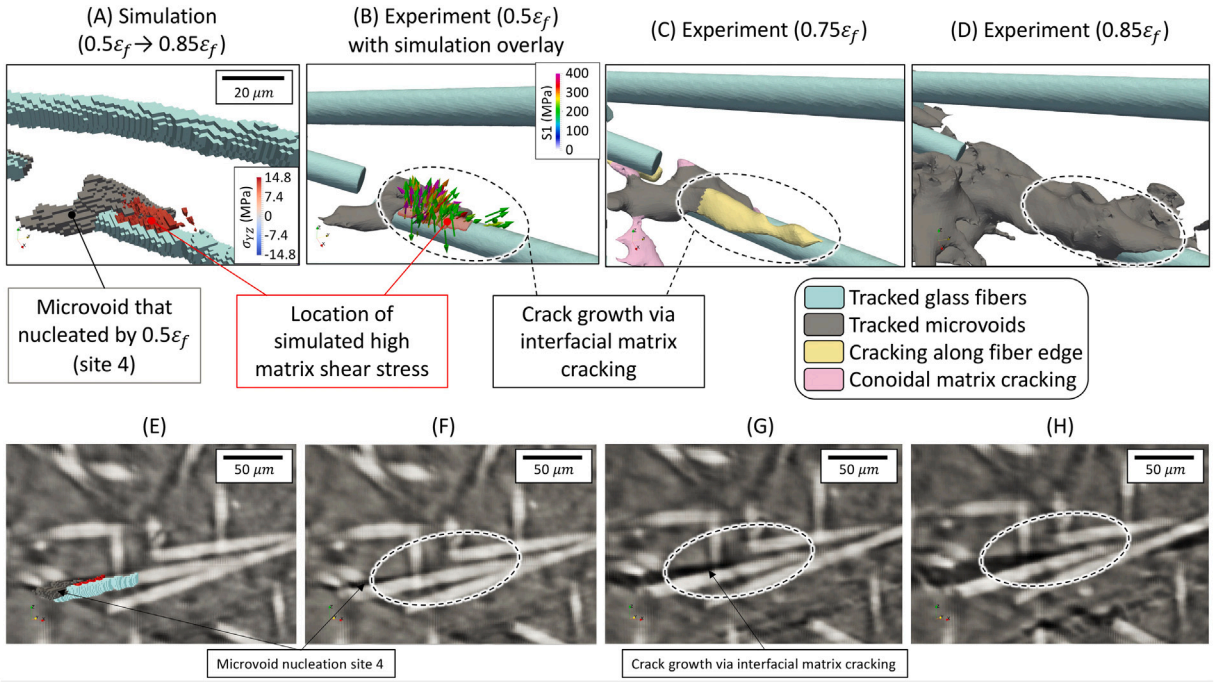

Fig. 5. The coupled simulation and experiment results of site 4 and 4A, where (A) shows the simulation result with the 99th percentile matrix shear stress (YZ) overlaid, (B) shows the coupled simulation and experiment at $0.5\varepsilon_f$ with the simulated maximum principal stress overlaid, and (C) and (D) show the 3D experimental results at $0.75\varepsilon_f$ and $0.85\varepsilon_f$, respectively. A different view of the same data with an intersecting plane is shown in (E), with the corresponding tomography images at those planes shown in (F), (G), and (H) at $0.5\varepsilon_f$, $0.75\varepsilon_f$, and $0.85\varepsilon_f$, respectively, where the dashed circle contains the region of high shear stress emanating from a microvoid which led to damage progression.

contraction in the XY plane that was experimentally observed between the unloaded state and $0.85\varepsilon_f$, while still allowing for rotations at nodes and lateral motion of each face in order to avoid fixing the internal surfaces. The simulation contained approximately 7.42 million elements, and was solved using Abaqus/Standard on 160 parallel processors and 512 GB of memory in 35 hours. The simulation was conducted with nlgeom=YES in Abaqus (which is best for non-linear deformation).

In the analysis of the simulation, hydrostatic stress was computed by

$$\sigma_{hyd} = \frac{\sigma_{xx} + \sigma_{yy} + \sigma_{zz}}{3} \tag{1}$$

and the maximum principal stress was computed by solving the eigenvalue problem

$$[\sigma_{ji} - \lambda\delta_{ij}]^T \hat{n}_j = 0 \tag{2}$$

where σ_{ji} is the stress tensor, δ_{ij} is the Kronecker delta, λ_1, λ_2, and λ_3 are the principal stresses (eigenvalues) and $\hat{n}_1$, $\hat{n}_2$, and $\hat{n}_3$ are the principal directions (eigenvectors) for the principal stresses, respectively. The maximum principal stress, S1, was then computed by $max(\lambda_1, \lambda_2, \lambda_3)$ and the direction of maximum principal stress was the corresponding eigenvector. The computations were conducted element by element in Matlab, and all visualizations of the simulation results were conducted in ParaView. It was found to be very useful to simultaneously render the raw tomography images, the segmentation of the tomography images (including fibers and voids), and the result of the simulation. This allowed for the ability to probe all three data sets for a robust analysis, using filters like the threshold filter, the slice filter, and the clip filter in ParaView.

It should be noted that this simulation did not include a damage model or a crack propagation model. Instead, regions of experimental damage were compared to the simulated stresses that are computed within the microstructure that is captured directly after $0.5\varepsilon_f$ in the tomography images. Therefore, this work does not simulate damage but instead uses computed stresses to further understand and distinguish the experimental damage behavior of each damage mechanism.

3. Results and discussion

Using the microstructural data at the unloaded state, it was found that the average weight based fiber length is approximately 300 μm and that fibers are moderately aligned with the loading direction forming an average angle of 40.4° with the Z axes [41,48]. From the time-lapse *in-situ* tomography data, it was found that damage initiation sites 4, 5, and 6 (Fig. 2) coalesced into a large void that reached the free surface. The experimental analysis, which tracked the microstructure as damage propagated, revealed that coalescence either occurred through cracking along a fiber edge (which could be interfacial cracking or debonding), or conoidal matrix cracking.

Experimentally, portions of damage events were determined to be cracking along fiber edges if the damage profile exhibited an elongated shape and was along the edge of a fiber, as determined by 3D visualization and oblique slicing of the tomography data in ParaView. As described in Section 1, since the thickness of the interphase is on the order of nanometers, it is much smaller than the 1.3 μm pixel size of the acquired tomography images. Therefore, interfacial matrix cracking and debonding visually appeared to have the same profile (cracking along fiber edges) in the *in-situ* tomography images. However, it will be shown that the computed stress states in the simulation provide insight into which of the two mechanisms were active. The experimental damage coalescence can be seen in Fig. 4, were experimental crack growth has been labeled as either along a fiber edge, or through the matrix. Specifically, experimental crack growth in Fig. 4 which has been labeled as 4A, 4B, 5A, and 6A will be explored in detail.

3.1. Interfacial matrix cracking and debonding

The first case that will be discussed is crack growth site 4A in Fig. 4, which facilitated the growth of crack initiation site 4 (microvoid nucleation) via a misaligned fiber forming an 80° angle with the loading axes. Experimentally, this region was observed to contain cracking along the fiber edge, shown circled in Fig. 5B–H. In the simulation, the local stress states were examined in the matrix elements at the matching

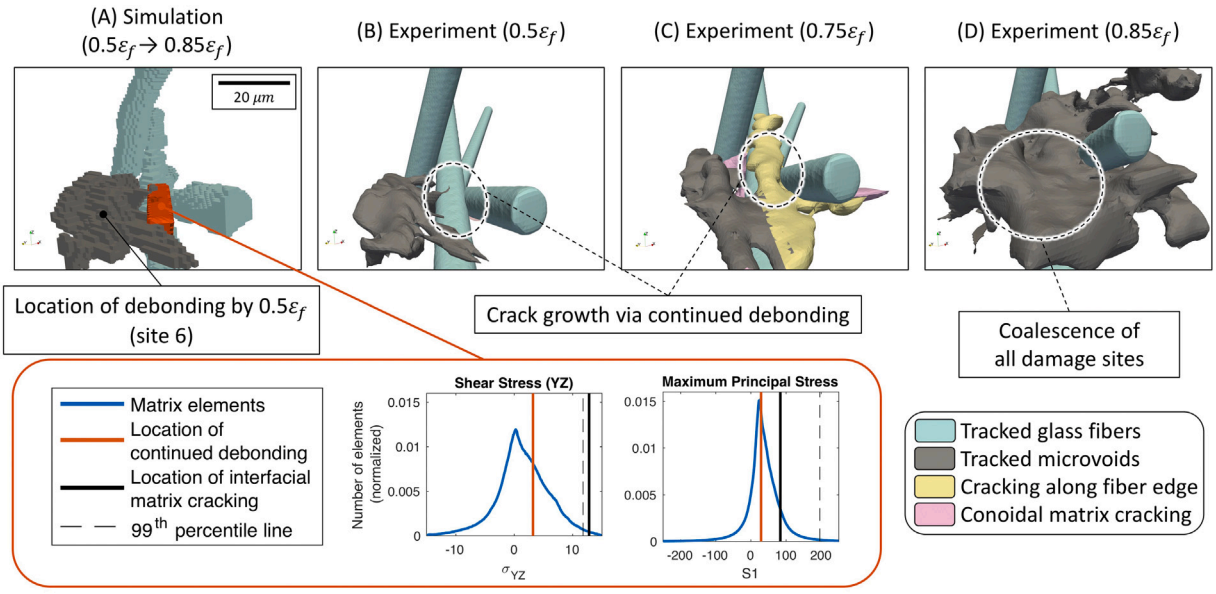

Fig. 6. The coupled simulation and experiment analysis of site 6 and 6A, where (A) shows the simulation, with the elements at the location of debonding shown in orange, accompanied by an inset providing a comparison of the stresses averaged over those elements and compared with the location of interfacial matrix cracking, and (B), (C), and (D) show the 3D experimental results at $0.5\varepsilon_f$, $0.75\varepsilon_f$ and $0.85\varepsilon_f$, respectively.

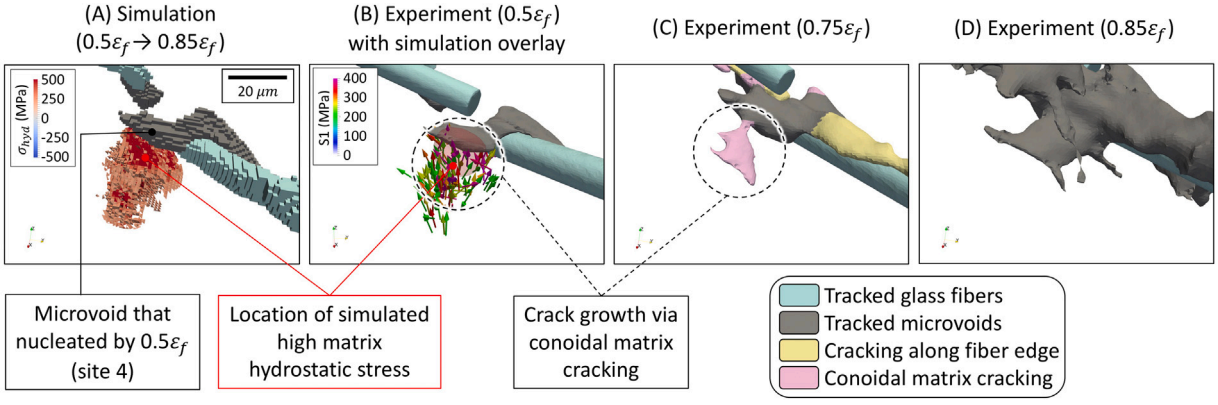

Fig. 7. The coupled simulation and experiment results at site 4 and 4B, where (A) shows the simulation result with the 99th percentile matrix hydrostatic stress overlaid, (B) shows the coupled simulation and experiment at $0.5\varepsilon_f$ with the simulated maximum principal stress overlaid, and (C) and (D) show the 3D experimental results at $0.75\varepsilon_f$ and $0.85\varepsilon_f$, respectively.

location. It was found that the stress state in the local matrix material at this location exhibited a notably high shear stress concentration in the YZ plane, σ_{YZ}, shown in Fig. 5A. In fact, this matrix region alone contained 866 agglomerated matrix elements all within the 99th percentile of matrix σ_{YZ} (where the matrix average σ_{YZ} was 1.47 MPa, and the 99th percentile σ_{YZ} was 11.77 MPa). While the fiber which facilitated this crack growth in Fig. 5 is not exactly aligned in the YZ plane, this correlation could be due to the boundary conditions discussed in Section 2.4, which imposed a compression (matching the experimental contraction due to Poisson's effect) in the X direction that was almost twice as large compared to the Y direction. This compression in the X direction, which is normal to the YZ plane, could explain why σ_{YZ} was very high at this site of cracking along the fiber edge.

Additionally, this region of high matrix shear stress also contained matrix elements with high (99th percentile) maximum principal stress (where the average S1 was 35.18 MPa and the 99th percentile S1 was 195.93 MPa) as shown in Fig. 5B. This high maximum principal stress is likely due to the effects of the local microstructure, which included fibers and the neighboring microvoid. Since the matrix material at this location (circled in Fig. 5) experienced high maximum principal stress and high shear stress, this location of damage propagation is most likely matrix mediated, and it can therefore be categorized as interfacial matrix cracking. Experimentally, this is consistent with the surface observations made by Sato et al. which showed that sites of microvoid nucleation propagate via micro-cracks in the matrix along fiber edges [19]. The coupled simulation in this work showed that localized high matrix maximum principal stress and matrix shear stress were responsible for damage propagation at a site of crack initiation in the form of interfacial matrix cracking.

This can be contrasted to cracking site 6A (Fig. 4) which propagated from damage initiation site 6 that was determined to be early debonding. A closeup view of this location can be seen in Fig. 6. Interestingly, at this location within the microstructure (shown in orange in Fig. 6A), there were no notable extremities in the matrix stress states. In comparison to the location of interfacial matrix cracking, the values of σ_{YZ} and maximum principal stress have been averaged and plotted for this location in the inset of Fig. 6A, where the lower values can be contrasted to the region of interfacial matrix cracking circled in Fig. 5, which showed relatively higher matrix σ_{YZ} and matrix maximum principal stress. Since the stresses in the matrix along the fiber in Fig. 6 were not high, it is reasonable to conclude that this

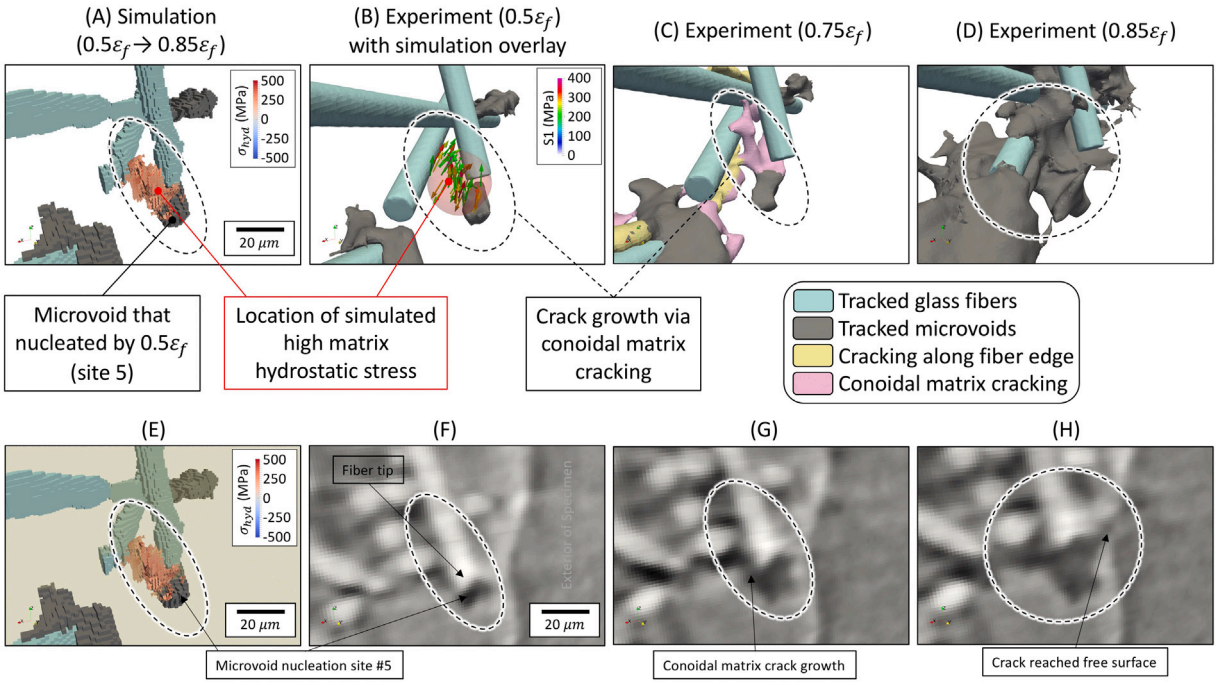

Fig. 8. The coupled simulation and experiment results at site 5 and 5A, where (A) shows the simulation result with the 99th percentile matrix hydrostatic stress overlaid, (B) shows the coupled simulation and experiment at $0.5\varepsilon_f$ with the simulated maximum principal stress overlaid, and (C) and (D) show the 3D experimental results at $0.75\varepsilon_f$ and $0.85\varepsilon_f$, respectively. A view of the same data with an intersecting plane is shown in (E), with the corresponding tomography image at that plane shown in (F), (G), and (H) at $0.5\varepsilon_f$, $0.75\varepsilon_f$, and $0.85\varepsilon_f$, respectively.

location of cracking along the fiber edge (during $\varepsilon > 0.5\varepsilon_f$) was not matrix mediated, but was instead in the form of continued debonding from the site of initial debonding that occurred during $\varepsilon < 0.5\varepsilon_f$ (akin to continued adhesive failure).

3.2. Conoidal matrix cracking

Another active mechanism during damage propagation that was observed experimentally was matrix driven conoidal cracking. The damage profile was characterized as matrix conoidal cracking (through 3D analysis and oblique slicing of the tomography data in ParaView) if it appeared that the crack grew in a conoidal shape, and not necessarily along an interface of a fiber edge, but in a tortuous manner through the fibrous microstructure.

One location within the microstructure that exhibited conoidal matrix cracking was also connected to the location of microvoid nucleation during damage initiation (site 4) discussed in Section 3.1. This cracking was labeled site 4B in Fig. 4, and a zoomed in view is provided in Fig. 7. The results of the simulation in this region contained 4038 agglomerated matrix elements all experiencing high (99th percentile) hydrostatic stress (where the average hydrostatic stress was 20.20 MPa and the 99th percentile of hydrostatic stress was 180.20 MPa), as shown in Fig. 7A. This agglomeration of matrix elements, while in close proximity to other fibers, was not along the edge of a single fiber.

These matrix elements with high hydrostatic stress were in contact with the surface of the microvoid, and were also experiencing high maximum principal stress (likely due to the neighboring microstructure), as shown in Fig. 7B. Experimentally, this region showed evidence of conoidal matrix cracking which occurred by $0.75\varepsilon_f$ as shown in Fig. 7C, and by $0.85\varepsilon_f$ coalesced into one void shown in Fig. 7D. This experimental analysis shows that matrix cracking can behave in a fiber-avoidance mode sub-surface, corroborating previous observations made using surface measurement techniques; the coupled simulation shows that it overlapped with a region of high hydrostatic stress emanating from a site of microvoid nucleation.

Another location within the microstructure that exhibited conoidal matrix cracking is shown in Fig. 8A and B. This location, labeled as site 5 in Fig. 2, exhibited a complicated fiber microstructure with highly misaligned fibers interacting with well aligned fibers during damage propagation. The simulation revealed 1163 agglomerated matrix elements experiencing high matrix hydrostatic stress (99th percentile matrix hydrostatic stress) shown in Fig. 8A and sliced in Fig. 8E.

Similar to the previous conoidal matrix cracking case, this location also experienced high maximum principal stress as shown in Fig. 8B. By $0.75\varepsilon_f$, the region showed damage progression in the form of conoidal matrix cracking, which was part of the large coalesced void by $0.85\varepsilon_f$. This location was particularly interesting because it was very close to the free surface of the specimen shown in Fig. 8F. By $0.85\varepsilon_f$, the local damage event coalesced with the other locations of damage described in this work, and reached the free surface eventually leading to catastrophic brittle failure as the ductile fracture zone eventually transitioned to brittle fracture [22].

3.3. High stress at pristine matrix regions

While this work focused on regions of experimental crack growth and compared the stresses simulated at those locations, it is also important to discuss regions of high simulated stress that were not associated with crack growth. These are regions of simulated stress that were away from the crack initiation sites (regions of the matrix that did not exhibit any signs of damage initiation by $0.5\varepsilon_f$) and will be referred to as pristine locations. These pristine locations at $\varepsilon < 0.5\varepsilon_f$ could either correspond to no experimental damage at $\varepsilon > 0.5\varepsilon_f$ and therefore remain pristine, or could possibly show signs of new experimental damage at $\varepsilon > 0.5\varepsilon_f$ (not associated with the crack growth in Fig. 4). Locations of 99th percentile shear and maximum principal stress ($\sigma_{YZ} > 11.8$ MPa and $S1 > 195.9$ MPa) were isolated and examined, as well as locations of 99th percentile hydrostatic and maximum principal stress ($\sigma_{hyd} > 180.2$ MPa and $S1 > 195.9$ MPa).

When matrix elements of high σ_{YZ} and high $S1$ were not touching crack initiation sites and instead were at pristine matrix locations,

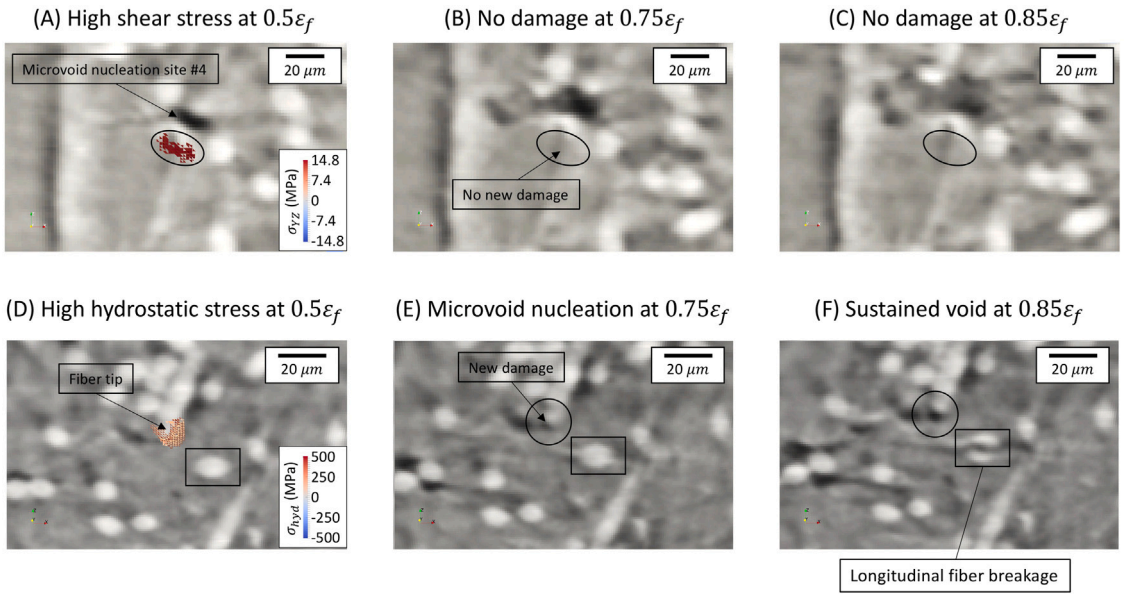

Fig. 9. A separate example of high simulated shear stress and high maximum principal stress is shown in (A) at $0.5\varepsilon_f$, with the experimental results at (B) $0.75\varepsilon_f$ and at (C) $0.85\varepsilon_f$ where it can be seen that the region was not related to damage, showing that while this shear stress condition can lead to crack growth of existing cracks, it does not result in crack initiation at pristine matrix locations. An example of high hydrostatic stress and high maximum principal stress at a fiber tip is shown in at (D) $0.5\varepsilon_f$, at (E) $0.75\varepsilon_f$, and at (F) $0.85\varepsilon_f$, where it can be seen that a microvoid has appeared, showing that this hydrostatic stress condition can lead to both crack growth of existing cracks, as well as crack initiation in pristine matrix regions. Shown in the box in D–F is a rare location of longitudinal fiber breakage that is also discussed in this work.

they were not found to correlate to damage. For example, Fig. 9A–C shows matrix elements of high shear and maximum principal stress that were not in contact with sites of damage initiation. As can be seen in Fig. 9B and C, no damage was initiated within the experimental tomography images. This example was representative of other regions of high shear stress and high maximum principal stress, which when in contact with existing crack initiation sites led to crack growth in the form of interfacial matrix cracking, but when isolated at locations of pristine matrix did not lead to new cracking.

On the other hand, matrix elements experiencing high hydrostatic and maximum principal stress at pristine matrix locations were found to overlap with the nucleation of new microvoids. This can be seen in Fig. 9D–F, where matrix elements that were simulated to experience high hydrostatic and high maximum principal stress were not in contact with sites of crack initiation, however those elements corresponded to a new microvoid at a fiber tip as shown in Fig. 9E and F. This example was representative of other regions of high hydrostatic and high maximum principal stress, which when in contact with existing crack initiation sites led to crack growth in the form of conoidal matrix cracking, and when isolated at locations of pristine matrix led to new microvoid nucleation.

The observations made by examining the results of the simulation at pristine matrix locations shed light on the underlying physical phenomena and stress states related to matrix damage. After crack initiation, high shear stress was only observed at the experimental locations of interfacial matrix cracking, and did not necessarily correspond to new damage in the tomography images at locations away from crack initiation sites (pristine locations). This indicates that while interfacial cracking is matrix mediated, the high stress conditions associated with it do not result in new cracks at additional locations away from the initial crack initiation site. On the other hand, high hydrostatic stress was both observed at the sites of crack growth in the form of conoidal matrix cracking, as well as the nucleation of new microvoids at previously pristine matrix locations. This implies that conoidal matrix cracking has the same physical driving force as the nucleation of new voids, indicating that conoidal matrix cracking can be viewed as the nucleation of a void in-contact with the site of crack initiation.

3.4. Fiber breakage

Fiber breakage in general has not been considered a common occurrence in short fiber thermoplastic composites. Furthermore, when observed, it is usually a transverse breakage of a well aligned fiber [22,35]. Out of the nearly 400 fibers in the ductile fracture zone, only one fiber breakage occurred by $0.5\varepsilon_f$ (shown in Fig. 2 at damage initiation site 2). This fiber was well aligned with the loading direction, forming a 17.6° angle with the loading direction, and broke via the more commonly expected transverse mode due to neighboring microvoid nucleation [22].

However, this analysis showed that between $0.5\varepsilon_f$ and $0.85\varepsilon_f$, five additional fibers broke, representing 1.5% of the total fibers in the ductile fracture zone. Of the five fiber breakage events that occurred between $0.5\varepsilon_f$ and $0.85\varepsilon_f$, four were transverse breaks of well aligned fibers, and one was a longitudinal break of an in-plane fiber. The longitudinal breakage event occurred at a fiber that was 241 μm long and was aligned almost perpendicular to the loading axes, forming an angle of 86° with the loading direction (Z).

The longitudinal fiber breakage event of the nearly in-plane fiber can be seen in Fig. 10A, B, C, and D at the unloaded state, $0.5\varepsilon_f$, $0.75\varepsilon_f$, and $0.85\varepsilon_f$, respectively, where the longitudinal break can be observed at $0.85\varepsilon_f$. This occurrence is unexpected because even with a pre-treatment of the fiber surface (which promotes adhesion with the matrix), the polypropylene matrix material has a much lower ultimate strength than the E-glass fiber [45,47]. Therefore, the matrix near the interface would be expected to fail first.

The simulation result showed that this fiber experienced a high shear stress gradient shown in the inset of Fig. 10B. Yet, this stress state was not unique to this fiber alone; almost all highly misaligned fibers in the microstructure were simulated to experience a similar shear stress gradient. Therefore, the longitudinal fiber break of this particular misaligned fiber was not only a result of its shear stress state, but was found to be a result of its morphology which was observed through a reconstruction of the exact fiber surface. Specifically, an in-depth surface reconstruction of the fiber showed that it was damaged at the unloaded state (Fig. 11A) likely due to environmental damage of the E-glass fiber [49]. The damage can be seen in the tomography images

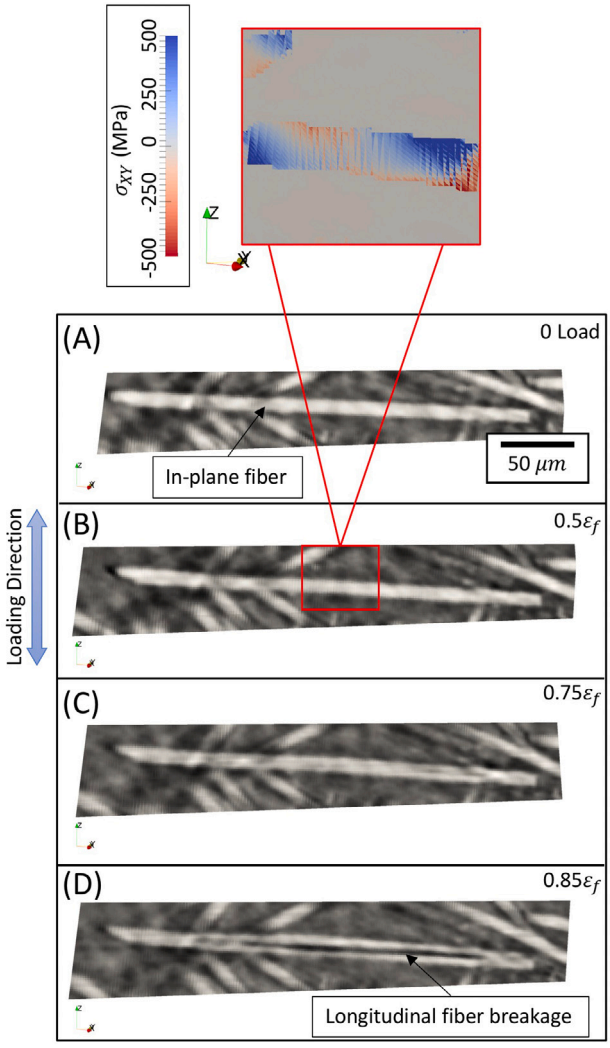

Fig. 10. Experimental data of the damaged in-plane (XY plane) fiber shown at (A) the unloaded state, (B) $0.5\varepsilon_f$, (C) $0.75\varepsilon_f$, and (D) $0.85\varepsilon_f$ where longitudinal fiber breakage has occurred, as well as an image of the simulated fiber experiencing a high shear stress gradient in its plane (XY plane).

at the oblique slices shown in Fig. 11B, where tomography images in slice one, two, and five have been circled and clearly show that the fiber is damaged in the unloaded state. It is important to note that fiber damage is challenging to detect and can be missed when observing tomography images in the orthogonal Cartesian planes; sometimes it is necessary to view an accurate surface reconstruction of the fiber, or view tomography data at oblique angles to observe the true morphology of certain features.

Overall, for this in-plane fiber (that was highly misaligned with the loading direction), it was found that the fiber surface pre-treatment used to promote adhesion with the matrix was very effective because there were no signs of debonding in the *in-situ* tomography images, as was seen in Fig. 10. With a strong bond to the matrix, it is therefore hypothesized that the highly misaligned fiber broke longitudinally because (1) it was damaged at the unloaded state likely due to the injection molding fabrication, and (2) it experienced a high shear stress gradient between $0.5\varepsilon_f$ and $0.85\varepsilon_f$, as was shown in Fig. 10D.

4. Conclusion

This work analyzed specific damage events that occurred in a short fiber reinforced thermoplastic composite. Specifically, the specimen studied in this work was an injection molded polypropylene that was reinforced with 30%, by weight, 10 μm diameter E-glass fibers which were pre-treated to promote adhesion between the fibers and the matrix. The experiment was an incremental tension test that was conducted *in-situ* where X-ray μ-CT images were acquired at a total of 58 interruptions between the unloaded state and failure, which occurred at 5.77% macroscopic strain (computed through digital image correlation of the speckled surface of the specimen during the *in-situ* experiment).

Analysis of the 3D tomography images was conducted to determine the ductile fracture zone just before brittle fracture occurred. Through 2D image correlation, the ductile fracture zone was traced back to the microstructure at the unloaded state. The progression of the microstructure was then studied in detail using a total of three detection procedures: fiber detection, void detection, and specimen edge detection. The 3D analysis revealed the exact locations of damage initiation within the ductile fracture zone, which were observed to occur by $0.5\varepsilon_f$. There were six independent sites of damage initiation: five sites of microvoid nucleation at fiber tips (discussed in the previous work) [22], and one site of debonding of two short highly misaligned fibers which occurred likely as a result of low adhesion with the matrix (since it was observed early in the loading sequence). In this work, the progression of these sites of damage after $0.5\varepsilon_f$ (crack growth) was analyzed.

Three of the six total locations of damage initiation (two microvoid nucleation sites and the one debonding site) were experimentally observed to coalesce into one connected void which reached the free surface by $0.85\varepsilon_f$ through either cracking along a fiber edge or conoidal matrix cracking. To understand the complex growth of cracking which caused large coalescence in the three sites of damage, a FEM simulation was conducted of the exact local microstructure as extracted through the three detection techniques described in this work. This region within the ductile fracture zone had a volume of 117 by 176.8 by 183.3 μm, and was tracked throughout the experimental loading history using six face 2D cross-correlation. The 3D simulation of this region of interest, which contained 89 tracked fibers and 7.42 million elements, was conducted to replicate the experimental boundary conditions experienced by the region.

Sites of early microvoid nucleation were found to propagate either through interfacial matrix cracking, or conoidal matrix cracking. At the region of interfacial matrix cracking, the simulation showed high matrix shear stress and maximum principal stress. This result substantiates the surface observations and hypothesized role of shear stress provided by Sato et al. in the growth of microvoids along fiber sides via microcracks in the matrix [19]. At the region of conoidal matrix cracking, the simulation showed that the matrix experienced high hydrostatic stress and maximum principal stress, causing the growth of the microvoid to occur through the matrix, and not necessarily along a fiber side.

The site of early debonding of two short fibers was found to propagate via continued debonding along a third fiber. The matrix stresses in the simulation at the location of debonding were not high (within one standard deviation of the average, as opposed to the extreme values in the shear and hydrostatic stresses observed for interfacial and conoidal matrix cracking, respectively), signaling that the event was not due to microcracks in the matrix, but instead likely due to adhesive failure of the interphase. This shows that both interfacial matrix cracking and debonding can occur within the microstructure during damage propagation. Lastly, five fiber breakage events were experimentally documented: four typical transverse fiber breaks of well aligned fibers, and one unlikely longitudinal fiber break of a highly misaligned fiber. The longitudinal fiber breakage event was further examined by extracting the exact morphology of the fiber at the unloaded state, which revealed that the fiber was damaged during the injection molding process, which likely led to its unexpected fracture behavior.

In conclusion, this work has provided clarity into the 3D damage propagation events of short fiber reinforced thermoplastics by

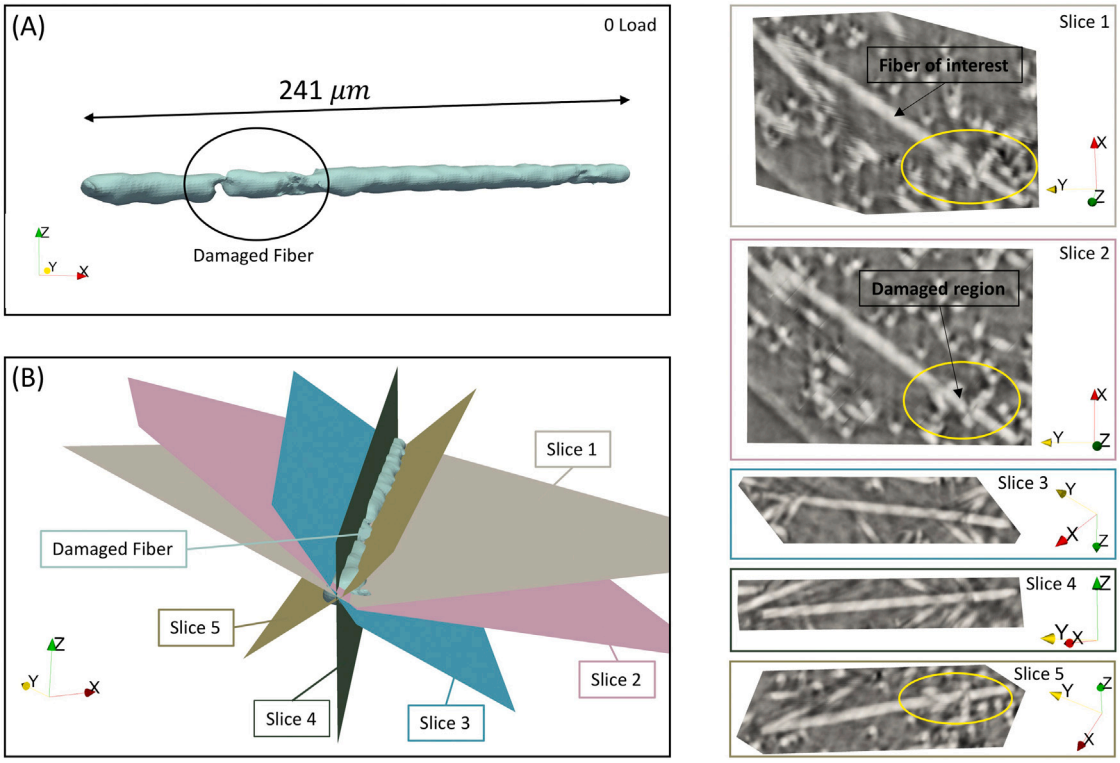

Fig. 11. The experimental data rendered at the unloaded configuration of an in-plane fiber (A) which was damaged during the injection molding process as can be seen circled, with accompanying tomography images sectioned at the five planes described in (B), where it can be seen circled in Slices 1, 2, and 5 that neighboring fibers appeared to have applied force during injection molding leading to damage in the fiber at the unloaded state.

providing insight into the physical phenomena that govern certain micromechanical behaviors. This includes the specific distinction between interfacial matrix cracking and debonding, as well as the roles of maximum principal stress, shear stress, and hydrostatic stress in the evolution of microvoids (crack growth in $\varepsilon > 0.5\varepsilon_f$) which nucleated during damage initiation ($\varepsilon < 0.5\varepsilon_f$). Specifically, using the criteria of high shear stress and maximum principal stress in the matrix, it was possible to isolate locations of incremental crack growth from a nucleated microvoid in the form of interfacial matrix cracking. However, this criteria in general cannot be used to determine new damage events at pristine matrix locations. Additionally, using the criteria of high hydrostatic stress and maximum principal stress, it was possible to isolate the path of incremental damage propagation from a nucleated microvoid in the form of conoidal matrix cracking, as well as the nucleation of new damage events in pristine matrix locations.

While this work identified critical trends using high stresses, future research could use coupled experiments and simulations to identify specific stress values that lead to certain damage events. This could be useful for exploring and estimating properties of the interphase. Additionally, predicting the locations of debonding remains an area of future research. This work showed that debonding initiated at two short in-plane fibers (≈50 μm long compared to the average ≈300 μm length) and propagated in the form of continued debonding along a third fiber. The relationship between the proximity of short in-plane fibers and the initiation of debonding is worth exploring in future work. Overall, this work provides a major step towards increasing predictive capabilities of the mechanical response of short fiber thermoplastic composites past the elastic regime, into the damage propagation regime, and eventually towards strength prediction and robust material qualification.

CRediT authorship contribution statement

Imad Hanhan: Methodology, Investigation, Formal analysis, Data curation, Visualization, Writing - original draft. **Michael D. Sangid:** Conceptualization, Resources, Supervision, Project administration, Funding acquisition, Writing - review & editing.

Declaration of competing interest

The authors declare that they have no known competing financial interests or personal relationships that could have appeared to influence the work reported in this paper.

Acknowledgments

The authors gratefully acknowledge support from the National Science Foundation CMMI MoM, Award No. 1662554. Partial support for I.H. was provided by the NSF GRFP, Award Number DGE-1333468. The authors would like to thank Ronald F. Agyei from Purdue University and Dr. Xianghui Xiao from Argonne National Laboratory for their help in acquiring the X-ray projections and in reconstructing the X-ray tomography images. The discontinuous fiber composite material was provided by Dr. Alan Wedgewood of Dupont. Use of the Advanced Photon Source was supported by the US Department of Energy, Office of Science, Office of Basic Energy Sciences, under contract No. DE-AC02-06CH11357.

References

[1] Ramani K, Bank D, Kraemer N. Effect of screw design on fiber damage in extrusion compounding and composite properties. Polym Compos 1995;16(3):258–66. http://dx.doi.org/10.1002/pc.750160310.
[2] Bailey R, Kraft H. A study of fibre attrition in the processing of long fibre reinforced thermoplastics. Int Polymer Process 1987;2(2):94–101.
[3] Stade K. Techniques for compounding glass fiber-reinforced thermoplastics. Polym Eng Sci 1977;17(1):50–7. http://dx.doi.org/10.1002/pen.760170110.
[4] Byron Pipes R, McCullough RL, Taggart DG. Behavior of discontinuous fiber composites: Fiber orientation. Polym Compos 1982;3(1):34–9. http://dx.doi.org/10.1002/pc.750030107.

[5] Gupta M, Wang KK. Fiber orientation and mechanical properties of short-fiber-reinforced injection-molded composites: Simulated and experimental results. Polym Compos 1993;14(5):367–82. http://dx.doi.org/10.1002/pc.750140503.

[6] Vaxman A, Narkis M, Siegmann A, Kenig S. Short-fiber-reinforced thermoplastics. Part III: Effect of fiber length on rheological properties and fiber orientation. Polymer Composites 1989;10(6):454–62. http://dx.doi.org/10.1002/pc.750100610, http://doi.wiley.com/10.1002/pc.750100610.

[7] Fu SY, Lauke B. Effects of fiber length and fiber orientation distributions on the tensile strength of short-fiber-reinforced polymers. Compos Sci Technol 1996;56(10):1179–90. http://dx.doi.org/10.1016/S0266-3538(96)00072-3.

[8] Connolly MP. The measurement of porosity in composite materials using infrared thermography. J Reinforced Plast Compos 1992;11:1367–75.

[9] Folgar F, Tucker CL. Orientation behavior of fibers in concentrated suspensions. J Reinforced Plast Compos 1984;3(2):98–119. http://dx.doi.org/10.1177/073168448400300201, http://jrp.sagepub.com/content/3/2/98.

[10] Phelps JH, Tucker CL. An anisotropic rotary diffusion model for fiber orientation in short- and long-fiber thermoplastics. J Non-Newton Fluid Mech 2009;156(3):165–76. http://dx.doi.org/10.1016/j.jnnfm.2008.08.002.

[11] Phelps JH, Abd El-Rahman AI, Kunc V, Tucker CL. A model for fiber length attrition in injection-molded long-fiber composites. Composites A 2013;51:11–21. http://dx.doi.org/10.1016/j.compositesa.2013.04.002.

[12] Tucker CL, Liang E. Stiffness predictions for unidirectional short-fiber composites. Compos Sci Technol 1999;59. http://dx.doi.org/10.1016/S0266-3538(98)00120-1.

[13] Nguyen BN, Bapanapalli SK, Holbery JD, Smith MT, Kunc V, Frame BJ, Phelps JH, Tucker CL, Tucker III CL. Fiber length and orientation in long-fiber injection-molded thermoplastics - Part I: Modeling of microstructure and elastic properties. J Compos Mater 2008;42(10):1003–29. http://dx.doi.org/10.1177/0021998308088606, http://jcm.sagepub.com/content/42/10/1003.abstract.

[14] Advani S, Tucker III C. The use of tensors to describe and predict fiber orientation in short fiber composites. J Rheol 1987;31(8):751–84. http://dx.doi.org/10.1122/1.549945.

[15] Eshelby J. The determination of the elastic field of an ellipsoidal inclusion, and related problems. Proc R Soc Lond. Ser A 1957;241(1226):376–96. http://dx.doi.org/10.1098/rspa.1957.0133, http://www.royalsocietypublishing.org/doi/10.1098/rspa.1957.0133.

[16] Matzenmiller A, Lubliner J, Taylor R. A constitutive model for anisotropic damage in fiber-composites. Mech Mater 1995;20(2):125–52. http://dx.doi.org/10.1016/0167-6636(94)00053-0.

[17] Kammoun S, Doghri I, Adam L, Robert G, Delannay L. First pseudo-grain failure model for inelastic composites with misaligned short fibers. Composites A 2011;42(12):1892–902. http://dx.doi.org/10.1016/j.compositesa.2011.08.013.

[18] Böhm HJ, Eckschlager A, Han W. Multi-inclusion unit cell models for metal matrix composites with randomly oriented discontinuous reinforcements. Comput Mater Sci 2002;25(1–2):42–53. http://dx.doi.org/10.1016/S0927-0256(02)00248-3.

[19] Sato N, Kurauchi T, Sato S, Kamigaito O. Microfailure behaviour of randomly dispersed short fibre reinforced thermoplastic composites obtained by direct SEM observation. J Mater Sci 1991;26(14):3891–8. http://dx.doi.org/10.1007/BF01184987.

[20] Bourmaud A, Ausias G, Lebrun G, Tachon ML, Baley C. Observation of the structure of a composite polypropylene/flax and damage mechanisms under stress. Ind Crops Prod 2013;43(1):225–36. http://dx.doi.org/10.1016/j.indcrop.2012.07.030.

[21] Modniks J, Andersons J. Modeling the non-linear deformation of a short-flax-fiber-reinforced polymer composite by orientation averaging. Composites B 2013;54(1):188–93. http://dx.doi.org/10.1016/j.compositesb.2013.04.058.

[22] Hanhan I, Agyei RF, Xiao X, Sangid MD. Predicting microstructural void nucleation in discontinuous fiber composites through coupled in-situ X-ray tomography experiments and simulations. Sci Rep 2020;10(1):3564. http://dx.doi.org/10.1038/s41598-020-60368-w, http://www.nature.com/articles/s41598-020-60368-w.

[23] Talreja R. Damage development in composites: Mechanisms and modelling. J Strain Anal 1989;24(4):215–22.

[24] Goh KL, Aspden RM, Hukins DW. Review: Finite element analysis of stress transfer in short-fibre composite materials. Compos Sci Technol 2004;64(9):1091–100. http://dx.doi.org/10.1016/j.compscitech.2003.11.003.

[25] DiBenedetto aT, DiBenedetto a. Tailoring of interfaces in glass fiber reinforced polymer composites: a review. Mater Sci Eng A 2001;302(1):74–82. http://dx.doi.org/10.1016/S0921-5093(00)01357-5.

[26] Gao S-l, Ma E. Characterisation of interphase nanoscale property variations in glass fibre reinforced polypropylene and epoxy resin composites. Composites 2002;33:559–76.

[27] Sato N, Kurauchi T, Sato S, Kamigaito O. Mechanism of fracture of short glass fibre-reinforced polyamide thermoplastic. J Mater Sci 1984;19(4):1145–52. http://dx.doi.org/10.1007/BF01120023.

[28] Huang H, Talreja R. Numerical simulation of matrix micro-cracking in short fiber reinforced polymer composites: Initiation and propagation. Compos Sci Technol 2006;66(15):2743–57. http://dx.doi.org/10.1016/j.compscitech.2006.03.013.

[29] Talreja R. Defect damage mechanics: Broader strategy for performance evaluation of composites. Plast Rubber Compos 2009;38(2–4):49–54. http://dx.doi.org/10.1179/174328909X387937.

[30] Selvadurai APS, Singh BM, Au MC. The matrix-fiber crack in an elastic solid. J Appl Mech 1996;63(3):639–49. http://dx.doi.org/10.1115/1.2823344, https://linkinghub.elsevier.com/retrieve/pii/S0045794904004262 https://asmedigitalcollection.asme.org/appliedmechanics/article/63/3/639/396365/The-MatrixFiber-Crack-in-an-Elastic-Solid.

[31] Horst JJ, Spoormaker JL. Fatigue fracture mechanisms and fractography of short-glassfibre-reinforced polyamide 6. J Mater Sci 1997;32(14):3641–51. http://dx.doi.org/10.1023/A:1018634530869.

[32] Sirivedin S, Fenner DN, Nath RB, Galiotis C. Matrix crack propagation criteria for model short-carbon fibre/epoxy composites. Compos Sci Technol 2000;60(15):2835–47. http://dx.doi.org/10.1016/S0266-3538(00)00167-6.

[33] Selvadurai AP, Ten Busschen A. Mechanics of the segmentation of an embedded fiber, part II: Computational modeling and comparisons. J Appl Mech Trans ASME 1995;62(1):98–107. http://dx.doi.org/10.1115/1.2895889.

[34] Notta-Cuvier D, Lauro F, Bennani B. Modelling of progressive fibre/matrix debonding in short-fibre reinforced composites up to failure. Int J Solids Struct 2015;66:140–50. http://dx.doi.org/10.1016/j.ijsolstr.2015.03.034.

[35] Rolland H, Saintier N, Robert G. Damage mechanisms in short glass fibre reinforced thermoplastic during in situ microtomography tensile tests. Composites B 2016;90:365–77. http://dx.doi.org/10.1016/j.compositesb.2015.12.021.

[36] Mullin J, Berry J, Gatti A. Some fundamental fracture mechanisms applicable to advanced filament reinforced composites. J Compos Mater 1968;2(1):82–103. http://dx.doi.org/10.1177/002199836800200107, http://journals.sagepub.com/doi/10.1177/002199836800200107.

[37] Gürsoy D, De Carlo F, Xiao X, Jacobsen C. Tomopy: A framework for the analysis of synchrotron tomographic data. J Synchrotron Radiat 2014;21(5):1188–93. http://dx.doi.org/10.1107/S1600577514013939.

[38] Dowd BA, Campbell GH, Marr RB, Nagarkar VV, Tipnis SV, Axe L, Siddons DP. In: Bonse U, editor. Developments in Synchrotron X-Ray Computed Microtomography at the National Synchrotron Light Source. 1999, p. 224–36. http://dx.doi.org/10.1117/12.363725.

[39] Pelt DM, Gürsoy D, Palenstijn WJ, Sijbers J, De Carlo F, Batenburg KJ. Integration of tomopy and the ASTRA toolbox for advanced processing and reconstruction of tomographic synchrotron data. J Synchrotron Radiat 2016;23(3):842–9. http://dx.doi.org/10.1107/S1600577516005658.

[40] Hanhan I, De Carlo F, Sangid M. Investigating surface and sub-surface damage in IM7/8552 via in-situ synchrotron X-ray computed tomography. In: AIAA Scitech 2020 Forum. Orlando, FL: American Institute of Aeronautics and Astronautics; 2020, p. 1–5. http://dx.doi.org/10.2514/6.2020-0248, https://arc.aiaa.org/doi/10.2514/6.2020-0248.

[41] Agyei RF, Sangid MD. A supervised iterative approach to 3D microstructure reconstruction from acquired tomographic data of heterogeneous fibrous systems. Compos Struct 2018;206:234–46. http://dx.doi.org/10.1016/j.compstruct.2018.08.029.

[42] Hanhan I, Sangid MD. Modlayer: A MATLAB GUI drawing segmentation tool for visualizing and classifying 3D data. Integr Mater Manufact Innov 2019;8(0123456789):468–75. http://dx.doi.org/10.1007/s40192-019-00160-5, http://link.springer.com/10.1007/s40192-019-00160-5.

[43] Arganda-Carreras I, Kaynig V, Rueden C, Eliceiri KW, Schindelin J, Cardona A, Seung HS. Trainable weka segmentation: A machine learning tool for microscopy pixel classification. Bioinformatics 2017;33(15):2424–6. http://dx.doi.org/10.1093/bioinformatics/btx180.

[44] Schindelin J, Arganda-Carreras I, Frise E, Kaynig V, Longair M, Pietzsch T, Preibisch S, Rueden C, Saalfeld S, Schmid B, Tinevez JY, White DJ, Hartenstein V, Eliceiri K, Tomancak P, Cardona A. Fiji: An open-source platform for biological-image analysis. Nat Methods 2012;9(7):676–82. http://dx.doi.org/10.1038/nmeth.2019.

[45] Agarwal BD, Broutman LJ, Chandrashekhara K. Analysis and Performance of Fiber Composites. John Wiley & Sons; 1990.

[46] Bauccio M. ASM Engineered Materials Reference Book. CRC; 1994.

[47] Mohammadpour E, Awang M, Kakooei S, Akil HM. Modeling the tensile stress–strain response of carbon nanotube/polypropylene nanocomposites using nonlinear representative volume element. Mater Des 2014;58:36–42. http://dx.doi.org/10.1016/j.matdes.2014.01.007.

[48] Hanhan I, Agyei R, Xiao X, Sangid MD. Comparing non-destructive 3D X-ray computed tomography with destructive optical microscopy for microstructural characterization of fiber reinforced composites. Compos Sci Technol 2019;184:107843. http://dx.doi.org/10.1016/j.compscitech.2019.107843, https://linkinghub.elsevier.com/retrieve/pii/S0266353819320925.

[49] Yilmazer U, Cansever M. Effects of processing conditions on the fiber length distribution and mechanical properties of glass fiber reinforced nylon-6. Polym Compos 2002;23(1):61–71. http://dx.doi.org/10.1002/pc.10412.